Edinburgh Research Explorer

Elbows of internal resistance rise curves in Li-ion cells

Elbows of internal resistance rise curves in Li-ion cells

Calum Strange[1], Shawn Li[1], Richard Gilchrist[1] and Gonçalo dos Reis[1,2]*

1   School of Mathematics, University of Edinburgh, Peter Guthrie Tait Road, Edinburgh, EH9 3FD, UK
2   Centro de Matemática e Aplicações (CMA), FCT, UNL, Portugal
*   Correspondence: G.dosReis@ed.ac.uk

1   **Abstract:** Degradation of lithium-ion cells with respect to increases of internal resistance (IR) has
2   negative implications for rapid charging protocols, thermal management of cells and power output.
3   Despite this, IR receives much less attention than capacity degradation in Li-ion cell research. Building
4   on recent developments on 'knee' identification for capacity degradation curves we propose the new
5   concept of 'elbow-point' and 'elbow-onset' for IR rise curves, and a robust identification algorithm
6   for those variables. We report on the relations between capacity's knees, IR's elbows and end of life
7   (EOL) for the large dataset of the study. We enhance our discussion with two applications. We use
8   Neural Network techniques to build independent State of Health capacity and IR predictor models
9   achieving a MAPE of 0.4% and 1.6%, respectively, and an overall RMSE below 0.0061. A relevance
10   vector machine (RVM) using the first 50-cycles of life data is employed for the early prediction of
11   elbow-points and elbow-onsets achieving a MAPE of 11.5% and 14.0% respectively.

12   **Keywords:** lithium-ion battery; internal resistance; elbow-points; early prediction; parameter
13   identification

1. Introduction

15   Sales of electric vehicles (EVs) and energy storage systems are undergoing a marked growth as
16   battery costs continue to fall and the introduction of increasingly strict regulations on CO2 and NOx
17   emissions, deadlines on the decommissioning of fossil fuel power stations, and bans on the sale of
18   internal combustion engines. Lithium-ion (Li-ion) batteries are widely deployed in EVs and energy
19   storage systems due to their outstanding characteristics such as lower maintenance requirements,
20   higher Coulombic efficiency and market-leading energy density. However, in operation, Li-ion batteries
21   undergo over-charging/discharging, high current stresses, over-temperature and under-temperature.
22   Even being cycled within moderate operating conditions, solid-electrolyte interphase (SEI) layer
23   growth on anodes gradually consumes active material, leading to poor cyclability. Extreme operating
24   conditions will further accelerate ageing processes, potentially resulting in high-risk failure scenarios
25   such as gassing, mechanical cracking of electrodes, internal short circuits and thermal runaway [1–9].
26   Further, the degradation rates of identical chemistry cells differ due to disparities in manufacturing
27   quality and operating conditions [2,10–12]. The accurate prognosis of cell degradation within the
28   battery pack is therefore imperative. This is referred to as the State of Health (SOH) of the cell, and
29   can be defined with respect to its capacity or its internal resistance (IR). A cell's capacity fades as its
30   calendar and cycle age increase, and degradation mechanisms take place within the cell that reduce
31   the available lithium inventory and accessible active material in the electrodes [13,14]. Conversely,
32   as the cell is cycled, IR increases due to the thickening formation of the SEI, and the consumption of
33   electrolyte and lithium in this process [1,2].
34   Given the importance of driving range, capacity is the primary SOH measurement for pure EVs.
35   However, capacity based SOH measurement is less important for hybrid electric vehicles (HEVs), since
36   HEVs demands high operating current to drive a heavier load than pure EVs. With the increase of

IR, the current deliverability of a cell is diminished, making IR a key SOH measurement for hybrid vehicles. With the increases of IR, cell voltage will raise sharply in the charging phase, and vice versa. As a result, the imposed current must be taped down to avoid the battery voltage from exceeding its maximum limit, leading to extended charging times and poor rapid charging ability [9,15–18]. In addition, the growth of IR values will incur more heat generation for given loads. As a result, the thermal management system of EV has to work harder to keep cells cool. To the best of our knowledge, the majority of EV manufacturers only provide a battery warranty securing that the capacity shall remain above 70% of its initial value, but ignore a battery warranty based on IR. With a greater understanding of expected IR growth, such warranties could be provided. There is thus significant value to be gained from the prognosis of IR growth trends. However, the prediction of IR degradation using data from early cycles remains largely unexplored. There is substantive research e.g. [19,20] conducted for early prediction of capacity but not for IR.

As discussed in-depth in [20], a cell's capacity does not degrade linearly throughout the cell's lifetime, degradation is path dependent [21], and a strong association exists between capacity and internal resistance [22]. Whilst the cell's capacity typically starts to degrade in a linear manner over the cell's cycle life, there eventually comes a point, called the 'knee-point', after which the rate of capacity degradation increases considerably [23–29]. In [20], one can find a review of knee-point identification methods in data [23,27,29], but crucially, the additional variable 'knee-onset' is introduced (along with an alternative identification mechanism) to provide a useful indication of the beginning of a sharp increase in the capacity degradation trend. The corresponding notion of 'knee-point' and 'knee-onset' in IR degradation curves is, to the best of our knowledge, absent from the literature. In this paper, we bridge this gap by addressing the IR rise curve and the corresponding change points: the 'elbow-onset' for when the IR curve starts being nonlinear, and the midpoint of the accelerated IR increase which we call the 'elbow-point'.

There are three main contributions of this work. Firstly, at a data preprocessing level, we create an accurate IR predictor utilising machine learning Convolutional Neural Network (CNN) techniques, this predictor used to complete the dataset of [30] for which no IR readings were logged. Secondly, underpinned by the completed dataset, the concepts of elbow-point and elbow-onset points for IR rise curves are proposed along with corresponding identification methods. Thirdly, we showcase a working example of using the predicted and real IR data for the early prediction of elbow-point and elbow-onset in the style of [20] using only the first 50-cycles of the cell's lifespan data.

The rest of this paper is organised as follows. Section 2 introduces the data pool and the data pre-processing approach addressing a missing IR data problem by employing a machine learning approach to predict the missing data. In Section 3, we propose the elbow-onset and -point concept and identification algorithms concluded by a study of the numerous relationships between these quantities. Section 4 presents the relevance vector machine (RVM) based machine learning approach for the early prediction of elbows. Results, contributions and future work are summarised in Section 5.

2. Battery data framework and data pre-processing procedures

2.1. Data description

We mainly work with the datasets of [19] and [30]. The data, its description and experimental details can be found at https://data.matr.io/1 (first and second blocks, respectively). Throughout this text, we will refer to the combination of these two datasets as the 'A123 dataset'. The data pool consists of high-throughput cycling data for eight batches of commercial *lithium iron phosphate (LFP)/graphite* cells cycled under fast-charging conditions: [19] provides data for three batches of approximately 48 cells each, here referred to as batches 1 to 3 (124 cells in total); [30] provides data for five batches of cells (233 cells in total), of between 45 and 48 cells each (here referred to as batches 4 to 8); batch 8 has 45 cells. *Cell code Notation*: across the 8 batches of cells in the A123 dataset, we refer to cell Y of batch X as $bXcY$.

All cells in batches 1, 2 and 3 are cycled to, or close to, their EOL, defined as 80% of initial capacity, in a temperature-controlled environment with a variety of charge/discharge profiles. It is important to note that for each individual cell, its charge/discharge profile was kept constant from cycle to cycle. Batches 4-7 were only cycled for 100-120 cycles and do not exhibit 'knees' nor reach EOL. Cells in batch 8 were cycled beyond their EOL. The dataset contains both in-cycle and per-cycle measurements. Discharge capacity, temperature, current and charge are logged at an in-cycle level, and per-cycle measurements of capacity, IR and charge time are provided. Data is recorded consistently from the second cycle. Contrary to batches 1–3, batches 4–8 contain no internal resistance measurements. The IR measurements provided are taken at a consistent Ah level of 80% state-of-charge (SOC) relative to nominal capacity. Throughout, we refer to this measurement as the IR of a cell. We note that the IR measurements for batches 1–3 contain a large amount of noise. [19] noted issues with their data logging equipment that affected some tests

2.2. Data pre-processing via a machine learning approach: completing the missing IR data

Our first goal, to increase the scope of our analysis, is to address the missing IR data of batch 8. We draw on machine learning techniques and build an IR prediction model (on the data from batches 1–3) to predict the missing IR data of batches 4-8. Increasing the number of matched capacity-IR curves from 124 pairs to 357(=124+233). Of these 357 pairs 169(=124+45) contain measurement up to or past the EOL. This will enhance our later analysis comparing elbows, knees and the EOL, as well as the early prediction of elbows. For statistical reasons we build a simple yet accurate capacity predictor to test for distributional dissimilarity between batches 1–3 and batches 4–8.

2.2.1. Pre-processing and modelling pipeline

We split the cells of the dataset into training and test sets, grouping by batch so that our test set contains an equal percentage of cells from each batch. As an input, our models take voltage, current and SOC data (the integral of the current, from one full cycle). This data was cleaned, standardised to have values between 0 and 1, interpolated using the *SciPy* [31] function *interp1d* to one measurement every four seconds and zero-extended so that the data for each cycle of each cell was of equal length and consistent time step. The median filter, averaging five nearest time instants, was applied to smooth the measurements of capacity and IR data prior to prediction.

To design our models for IR and capacity prediction, we utilised *K*-fold cross validation. A validation set of cells was chosen at random from the training set. Our models were fitted to the remaining training set, and evaluated on the validation set throughout training. This step was then repeated *K*-times with a new validation set and corresponding model. The average performance of the validation sets was used to optimise model design and choice of hyper-parameters. *K*-fold cross validation is particularly useful when working with small datasets, mitigating the risk of over-fitting a particular validation set [32]. After settling on the model's architecture and hyper-parameters (described next), a copy of the model was fitted to the whole training set and then evaluated on the test set.

2.2.2. Model for IR prediction

We propose a model consisting of a convolutional 'feature extraction' block followed by two densely connected layers displayed in Fig. 1 and described in Table 1. Our model was implemented in Python using TensorFlow via the Keras API [33]. All layer names given in Table 1 refer to the corresponding Keras layers. The model was trained on the data from batches b1–b3, using the *adam* optimiser for 50 epochs with a batch size of 526, and the *mean absolute error*, Eq. (1), as its loss function.
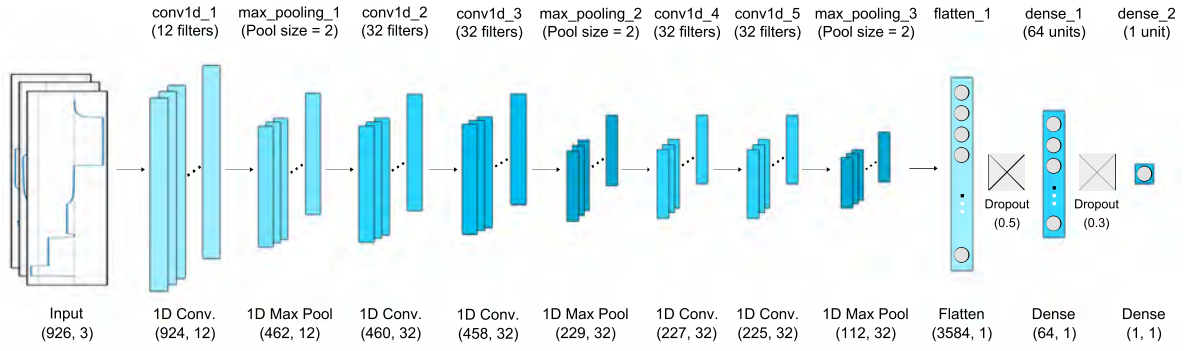
Figure 1. Schematic of machine learning model for IR prediction.

layer name	input size	hyper-parameters	output size
conv1d_1	926×3	12, 3, *ReLU*	924×12
max_pooling_1	924×12	2	462×12
conv1d_2	462×12	32, 3, *ReLU*	460×32
conv1d_3	460×32	32, 3, *ReLU*	458×32
max_pooling_2	458×32	2	229×32
conv1d_4	229×32	32, 3, *ReLU*	227×32
conv1d_5	227×32	32, 3, *ReLU*	225×32
max_pooling_3	225×32	2	112×32
flatten_1	112×32	-	3584
dropout_1	3584	0.5	3584
dense_1	3584	64, *ReLU*	64
dropout_2	64	0.3	64
dense_2	64	1, *linear*	1

Table 1. Proposed architecture of CNN model for prediction of IR. Hyper-parameters are given in the format: filters, kernel size, activation for conv1d layers; pool size for max_pooling; dropout for dropout; nodes, activation for dense layers.

Machine learning performance scores selected for this work are the mean absolute error (MAE), mean absolute percentage error (MAPE) and root mean square error (RMSE) defined as follows, for $\boldsymbol{y}$ the vector of true values and $\hat{\boldsymbol{y}}$ the vector of predicted values:

$$\mathrm{MAE}(\boldsymbol{y}, \hat{\boldsymbol{y}}) = \frac{1}{n_{\mathrm{samples}}} \sum_{i=1}^{n_{\mathrm{samples}}} |\hat{y}_i - y_i| , \qquad \mathrm{MAPE}(\boldsymbol{y}, \hat{\boldsymbol{y}}) = \frac{100\%}{n_{\mathrm{samples}}} \sum_{i=1}^{n_{\mathrm{samples}}} \frac{|\hat{y}_i - y_i|}{y_i} , \quad (1)$$

$$\text{and} \quad \mathrm{RMSE}(\boldsymbol{y}, \hat{\boldsymbol{y}}) = \sqrt{\frac{1}{n_{\mathrm{samples}}} \sum_{i=1}^{n_{\mathrm{samples}}} (\hat{y}_i - y_i)^2} . \qquad (2)$$

Our model's performance metrics for IR prediction can be found in Table 2. We are unaware of works using the A123 dataset for IR estimation. Nonetheless, as mentioned, the estimation of IR has been addressed [34,34–40]. We obtain a RMSE of 0.00035 and MAPE of 1.6% for IR (Table 2) which is low (if nominally compared with capacity estimation accuracy in the literature).

	RMSE		MAPE (%)	
	Train	Test	Train	Test
IR	$0.00029 \pm 6.2\mathrm{e}{-5}$	$0.00035 \pm 5.0\mathrm{e}{-5}$	1.19 ± 0.22	1.60 ± 0.24

Table 2. Average performance of model to predict IR, with 95% prediction intervals.

2.2.3. Validation step via a model for capacity prediction

We have shown that our model for IR prediction is effective on batches 1 − 3. To see if we can trust the predictions this model makes on batches 4 − 8 we check for non-similarity between the datasets. We do this by extrapolating on capacity, a variable present for all batches. This is a standard process in imputation (simple or multiple). To this end, we utilised a simple feed-forward neural network, consisting of three densely-connected layers. The first two layers containing 32 neurons with the rectified linear unit (ReLU) activation function, and the final layer consisting of a single neuron with a linear activation. The model was trained for 100 epochs with a batch size of 512, using the *adam* optimiser and the *mean squared error* as its loss function. During training, a dropout of 0.2 was utilised between the middle and last layer. Trained on all of the data from batches 1 − 3 and tested on batches 4 − 8 the model obtained the performance metrics displayed in Table 3 with an MAPE of 0.51%. This test gives us confidence that both datasets [19] and [30] are indeed not-dissimilar.

	RMSE		MAPE (%)	
	Train	Test	Train	Test
Capacity	$0.0053 \pm 4.2e-3$	$0.0095 \pm 4.6e-3$	0.37 ± 0.30	0.51 ± 0.26

Table 3. Average performance of capacity model trained on batches 1-3 tested on batches 4-8, with 95% prediction intervals.

The prediction of capacity (and SOH) is of wider interest than our discussion of elbows so we briefly compare these results with those found in the literature. We point to [41, Table 1] (MAPE and RMSE error given) and [42, Table 2] (error type not given) for a review/comparative work on capacity estimation. We cannot directly compare our results *as the data is different*. However, from a strictly numerical point of view, our RMSE of 0.0095 and MAPE 0.51% errors for capacity (Table 3) are lower than the values of [41, Table 1] – for a fair comparison one would need to test the varying approaches on a common dataset.

2.2.4. Predicting the missing IR data

In order to address the missing data issue, we trained the IR model on batches 1–3 multiple times and an ensemble of these models was used to predict on batches 4–8. This predicted IR data is available at https://doi.org/10.7488/ds/2957. Fig. 2 shows the IR for sample cell b8c4 and we strongly emphasise to the reader that the extrapolation of the IR data past EOL (80% capacity) is, as fully expected, not reliable: this stems from the limitation of the training dataset (batches 1–3) with data only up to the EOL point. Prediction outside that range of input data is not reliable as can be seen in Fig. 2 where we observe a strong widening in the prediction intervals[1] past the EOL.

2.2.5. Algorithmic framework

The proposed algorithmic framework can fully take advantage of machine learning-based approaches to solve the missing IR data problem in the raw data pool and allows the generation of artificial IR data to complete the life cycle data. The predicted IR data can be used for elbow-point and -onset identification and is able to assist the early prediction of the elbow-point and elbow-onset in IR curves.

The schematic framework of the employed algorithms is illustrated in Fig.2, where Section 2 introduces the data pre-processing procedure. In this regard, a CNN based predictor has been

---

[1] Prediction intervals provided throughout this text are calculated in a frequentist manner. A given model is fitted to data multiple times and performance metrics/predictions recorded. The empirical average and variance-value of predictions are calculated and under the assumption of normality one uses those values to produce prediction intervals (at any given probability quantile level q, e.g. in Fig. 2 we have $q = 95\%$ and $q = 80\%$).
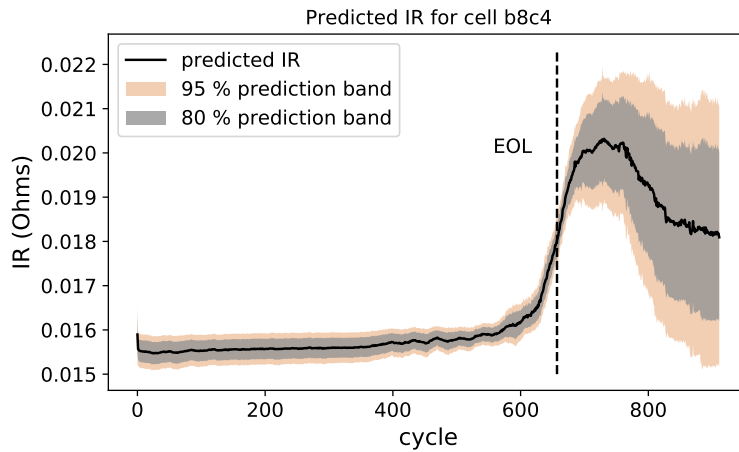
Figure 2. The predicted IR data for cell b8c4 is given by the black continuous line and is formed from the average of 20 predictions. We display 80% and 95% prediction intervals. Beyond the intuition of extrapolation, these intervals show that predictions past the EOL (capacity) should not be trusted.

trained on the data from batches 1–3 to predict the IR. In order to validate the CNN based predictor's application to batches 4–8, a separate model was trained on data from batches 1–3 to predict the capacity and tested on the measured capacity values for batches 4–8. Afterwards, the established predictor is used for IR predictions, completing the missing IR for batches 4–8. In Section 3, the completed life cycle data can be thus used for the identification of knee/elbow-point and -onset. By the analysis of the obtained knee/elbow-points and -onsets, we confirm the significant linear relationships between knee/elbow-points, -onsets and EOL. Further tests are carried out in Section 4 relating to the early prediction of elbow-points and -onsets based on our completed life cycle data with predicted IR. In particular, the straightforward Relevance Vector Machine (RVM) based quantitative method is applied to that completed battery dataset and produces the early predictions.
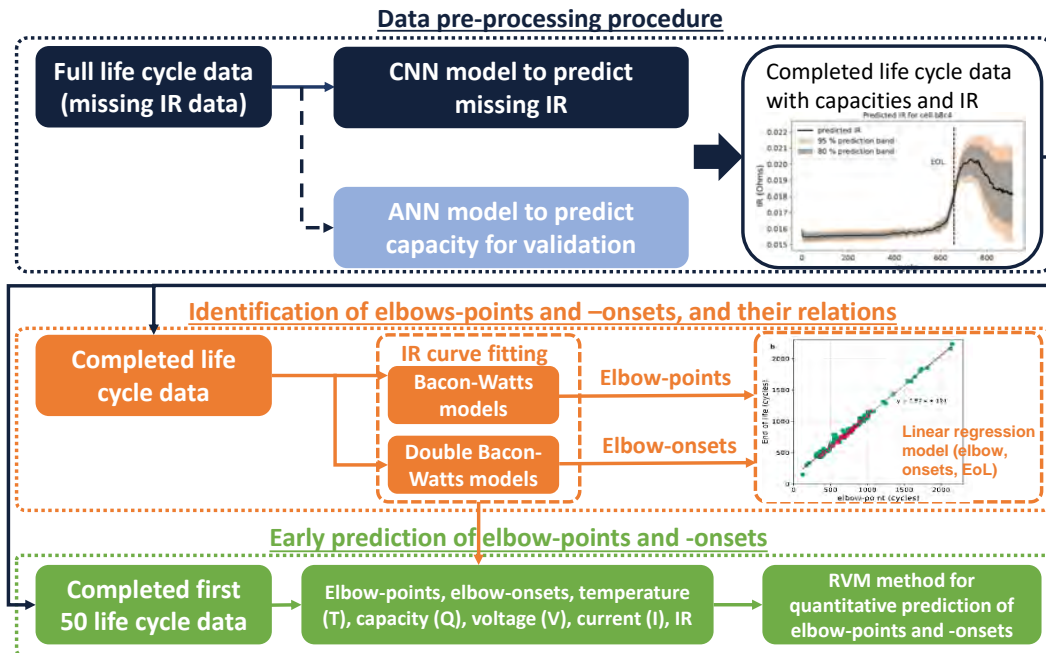
Figure 3. Graphical abstract for the proposed algorithmic framework

3. Identification of elbows, knees and their relations

3.1. Methodology

Fermin et. al. [20] proposed the use of the *Bacon-Watts* (Eq. (5)) and the *double Bacon-Watts model* (Eq. (6)) for identification of knee-point and knee-onset respectively. We will use the same methodology, with the addition of several steps to account for noise in the data and potential sigmoid behaviour. This noise, see Fig. 4a and Fig. 5a, prevents the Bacon-Watts model from neatly fitting the data as in [20] and this is overcome via a smoothing step as described in Algorithm 1 (block 1) below. We report that this noise also causes issues for the alternative knee identification methods proposed in [20,23,27], see Fig. 5. In addition, we observed sigmoid-type capacity fade curves for some cells in batch 8, and hence, we employ a subroutine to isolate the knee/elbow identification from the right-most plateau. We present first the algorithm and afterwards reason its several steps.

Algorithm 1 '*Smoothed Bacon-Watts*': Identification of knee/elbow-point and -onset

---

Block 1: *Data smoothing*

1. Fit isotonic regression to (capacity/IR degradation) lifespan data (across the full curve).
2. Determine data-truncation cycle-point n^*:

   (a) Fit (3) (Asymmetrical sigmoidal) to isotonic regression curve,
   (b) Find cycle-number, n^*; cycle at which 2nd derivative of fitted (3) changes sign, else last cycle in series.

3. Fit (4) (line-plus-exponential) to isotonic regression curve up to cycle n^*.

Block 2: *Identification*

4. Fit Bacon and Watts model (5) to (4). Identify knee/elbow-point.
5. Fit Double-Bacon and Watts model (6) to (4). Identify knee/elbow-onset.

The *isotonic regression step, Step 1*, solves several issues: it annuls the behaviour of capacity increase or IR decrease across the first few cycles and removes the influence of sharp movements where the IR decreases or increases due to measurement errors. From first principles, our choice reflects the fact that the electrochemical degradation mechanisms within the cell are *irreversible*. For a given load and set of ambient conditions, IR increase may be caused by the thickening of the SEI on the anode, which irreversibly consumes lithium and electrolyte. Additionally, IR increase can be caused by loss of anode and cathode material, which can be caused by many factors including electrode particle cracking and loss of electrical contact as a result of mechanical expansion and contraction upon cycling; corrosion of current collectors at low cell voltage; and binder decomposition at high cell voltage. These same mechanisms also lead to an irreversible reduction in capacity and, as such, the monotonicity of the model is also reflective of the real-world evolution of a cell's capacity over its lifespan. The isotonic regression is performed using the Scikit-learn Python package [43] and the procedure is described in [44].

The *Asymmetrical sigmoidal fitting step, Step 2*. The *Asymmetrical sigmoidal* ('as') model is described by Eq. (3)

$$Y^{as} = d + \frac{a - d}{\left[1 + \left(\frac{x}{c}\right)^b\right]^m} + \varepsilon^{as}, \tag{3}$$

where ε^{as} denotes the residuals[2] , and a, d associate to the top and bottom plateau of the curve respectively, b controls the slope between plateaus and m controls the level of asymmetry, lastly, c determines the inflexion point. For given data, the constants are estimated by straightforward least-squares estimation (also throughout the work for other models).

In several cells from batch 8 we observe a sigmoid-type capacity fade curve where, after passing the knee and then degrading linearly for some time, the degradation approaches a plateau (e.g. cell b8c4). To isolate the detection of knees/elbows from this behaviour we propose the fitting of the asymmetrical sigmoidal model to then truncate the data before said plateau (point n^*) via the 2nd derivative truncation rule.

The final *smoothing step, Step 3,* involves fitting the parametric *line-plus-exponential* ('*le*') model of Eq. (4) to the isotonic data (from Step 2) up to cycle n^*. This idea can be traced back to [45, Section 2.2.1] under the name of *Exponential/linear hybrid model* – [37,46] discuss other parametric models. The line-plus-exponential is described by the following model:

$$Y^{le} = \beta_0 + \beta_1 x + \beta_2 \exp(\lambda x - \theta) + \varepsilon^{le}, \tag{4}$$

where ε^{le} denotes the residuals, and β_0, β_1 and β_2 control the intersection point, and slope of the line and the size of the exponential, respectively. The quantity λ controls the 'speed' of the exponential and θ controls where the impact of the exponential starts. The main motivation for model (4) is that for many cells the degradation of IR is very close to linear (including the zero-slope case) until close to the elbow-onset followed by a sharp elbow-point.

For the *Bacon-Watts methodology, Step 4 & 5,* [20, Eq. (1)] describe the Bacon-Watts ('*bw*') model (5), as a two straight-line relationships around the transition point x_1:

$$Y^{bw} = \alpha_0 + \alpha_1(x - x_1) + \alpha_2(x - x_1) \tanh\{(x - x_1)/\gamma\} + \varepsilon^{bw}, \tag{5}$$

where ε^{bw} denotes the residuals α_0, α_1 and α_2 control the slopes of the intersecting lines and the intercept-weigh of the leftmost segment respectively, and γ controls the abruptness of the transition. γ is fixed as a small value to obtain an abrupt transition. After optimisation, the fitted value of x_1 is defined as the knee/elbow-point.

The identification of the knee/elbow-onset is done via the *double Bacon-Watts model ('dbw')* (6) (also [20, Eq. (2)]) by modifying Bacon-Watts to identify two transition points, concretely:

$$Y^{dbw} = \hat{\alpha}_0 + \hat{\alpha}_1(x - x_0) + \hat{\alpha}_2(x - x_0) \tanh\{(x - x_0)/\hat{\gamma}\} + \hat{\alpha}_3(x - x_2) \tanh\{(x - x_2)/\hat{\gamma}\} + \varepsilon^{dbw}, \tag{6}$$

as in equation (5), ε^{dbw} denotes the residuals, the parameters $\hat{\alpha}_i$ and x_j are estimated, and $\hat{\gamma}$ is chosen as a small value to produce abrupt transitions at x_0 and x_2. The *knee/elbow-onset is defined as the change point x_0.*

Fig. 4 displays the output of Algorithm 1 applied to the IR curve of cell b1c29 (non-predicted data). Elbow-point and its onset are identified, and the smoothing steps are illustrated showing the fitted isotonic regression and line-plus-exponential model against the input data (for this cell, Step 2 yields n^* as the final cycle number). Fig. 5 displays the performance of other known algorithms for knee identification applied to the elbow identification problem, finding that [20,23,27]'s algorithms are too sensitive to noise to provide consistent identification results. Our approach addresses the noise issue, allowing for coherent elbow identification throughout all curves. From a statistical point of view, any identification approach will be affected by the noise in the data. Thus, the identified elbows will be less exact than the knee identification where the data is much smoother. For comparison,

---

2   Throughout the manuscript, the generic $\varepsilon^{\cdot}$ denotes the errors/residuals of its associated model and is a normal random variable with zero mean and finite (but unknown) variance.

231   the non-parametric bootstrap procedure was used to calculate 95% confidence intervals (CI) for the
232   knee/elbow-points and -onsets identified by Algorithim 1. The average CI's width was 24 cycles
233   for the elbow-point, 4 cycles for the knee-point, 35 cycles for the elbow-onset and 5 cycles for the
234   knee-onset; this difference is a direct consequence of the noise present in the IR data. Finally, Algorithm
235   1 applied to knee identification recovers fully the results of [20]; we omit these results.
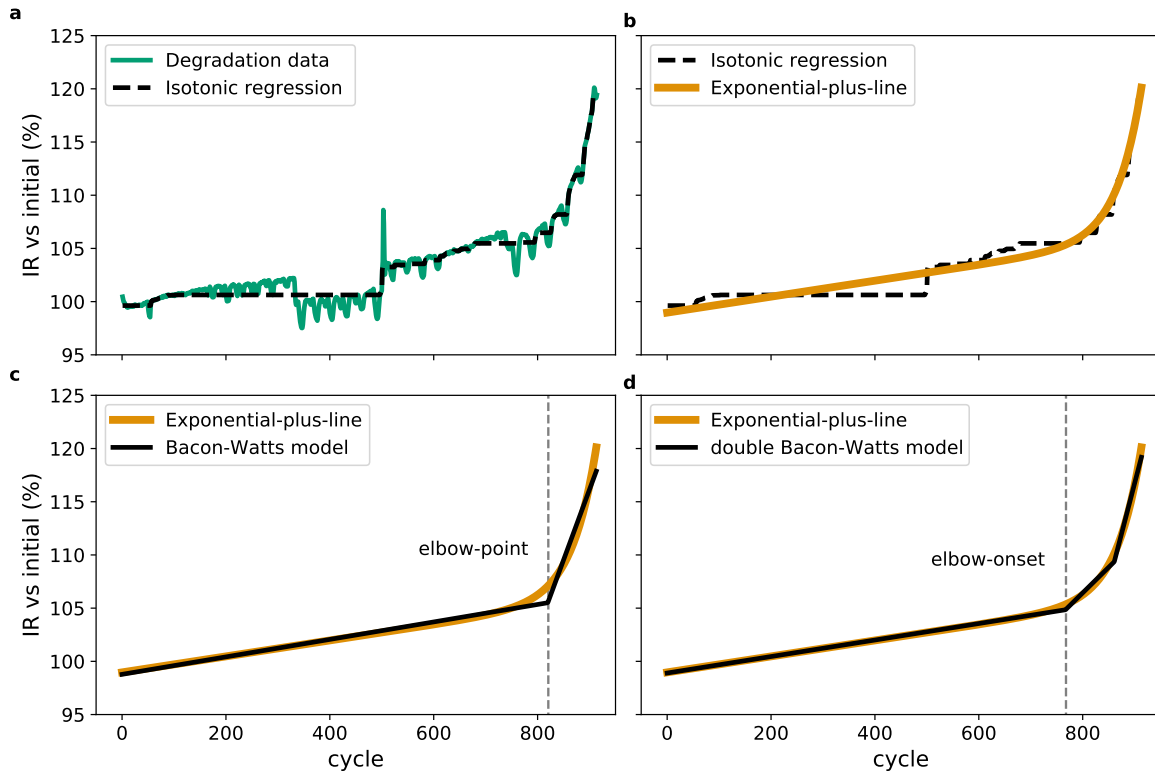
Figure 4. Steps of Algorithm 1 applied to the internal resistance degradation curve of cell b1c29 in the A123 dataset (non-predicted data). **a**, step 1. **b**, step 3. **c**, step 4. **d**, step 5. Step 2 is omitted as it has no impact here since n^* is chosen as the final cycle number. The width of the 95% confidence interval (computed by the non-parametric bootstrapping procedure) for the elbow-point of this curve is 23 cycles, and for the elbow-onset it is 38 cycles.
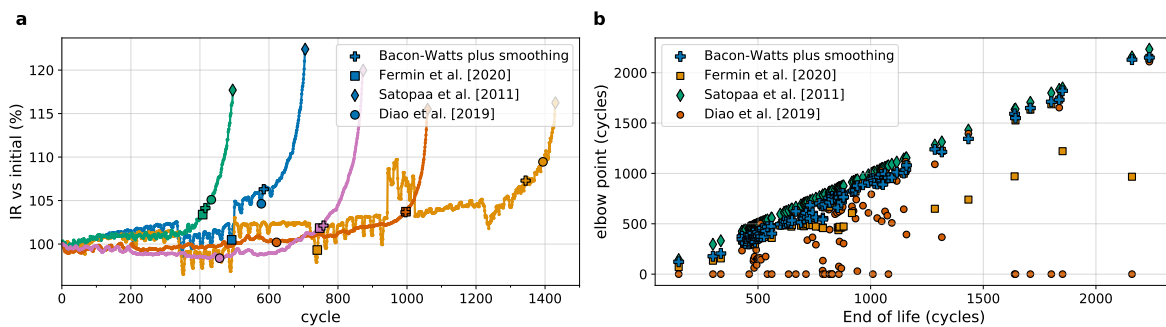
Figure 5. a, Comparison of elbow-points obtained with Algorithm 1, [20]'s Bacon-Watts, maximum curvature and slope changing ratio methods on a sample of cells from the A123 dataset (from left to right b2c34, b1c30, b3c15, b3c1, b1c3). **b**, Comparison of elbow-points for all cells in the A123 dataset. One expects to see a linear relationship between EOL and elbow-point; of the methods compared only Algorithm 1 and the algorithm of Satopaa et. al. [2011] recover a linear relationship reliably, however, by examining plot **a** we see that Satopaa's algorithm selects the end point as the elbow.

Zhang et al [29] report for a dataset of nickel-manganese-cobalt cells that the knee-point appeared at between 90 - 95% nominal capacity; in [20] it was reported that the knee-point for batches 1 to 3 of the A123 dataset, appeared on average at 95% nominal capacity and the knee-onset at 97.1% nominal capacity, with an average gap of 108 cycles between the knee and its onset. In this work, we report that, for the A123 dataset Batches 1, 2, 3 & 8, on average, the elbow-onset appears at 103.0% initial IR (93.6% nominal capacity) and the elbow-point at 104.7% initial IR (91.3% nominal capacity), with the elbow-onset and its point on average 52 cycles apart; on average both elbows appear after the knee-point. These reported figures are calculated from the smoothed exponential curve as described in Algorithm 1.

3.2. Linear relations

Figure 6 illustrates the strong linear relationships observed between the calculated knee/elbow-points and the EOL. Making it possible to estimate each point given a measurement or prediction of another point(s). These linear relations are obtained using a standard linear regression model $Y = c_0 + c_1 x + \varepsilon$ where Y denotes the dependent variable, x the independent variable, ε representing the residuals, and c_0 and c_1 control the intercept and slope of the linear model. The obtained coefficient values along with their confidence intervals are presented in Table 4, where the knee relations agree with those found in [20, Table 1].

We present the linear relationships obtained when including the predicted IR data. From viewing Fig. 6, comparing the green squares and black circles, the reader will appreciate that their inclusion did not significantly influence the linear relationship obtained. This observation lends a second layer of credibility to the predicted IR data, in that the elbows displayed in the predicted IR match closely with what one would expect given the linear relationships observed on batches 1–3.

(a) knee-point to EOL

Coefficient	Estimate	p-value
Intercept (β_0)	17 ± 21	
Slope (β_1)	1.26 ± 0.04	4.0×10^{-148}
EOL = 1.26 × knee-point + 17		

(b) elbow-point to EOL

Coefficient	Estimate	p-value
Intercept (β_0)	121 ± 11	
Slope (β_1)	0.97 ± 0.02	4.5×10^{-162}
EOL = 0.97 × elbow-point + 121		

(c) knee-point to elbow-point

Coefficient	Estimate	p-value
Intercept (β_0)	-103 ± 28	
Slope (β_1)	1.30 ± 0.05	3.6×10^{-147}
elbow-point = 1.30 × knee-point − 103		

(d) knee-onset to elbow-onset

Coefficient	Estimate	p-value
Intercept (β_0)	-143 ± 42	
Slope (β_1)	1.51 ± 0.08	4.5×10^{-112}
elbow-onset = 1.51 × knee-onset − 143		

Table 4. Coefficients of four linear regression models relating the knee-point (**a**) and the elbow-point (**b**) to the End of life, the knee-point to the elbow-point (**c**) and the knee-onset to elbow-onset (**d**) respectively. The *p*-values for β_1 were computed using the Wald test, and the small values allow the rejection of the null hypothesis that a linear relationship does not exist. The 95% confidence intervals for the estimated coefficients are calculated via bootstrapping. The coefficient of determination, R^2, of these linear regression models is (**a**) 0.9822, (**b**) 0.9896, (**c**) 0.9818 and (**d**) 0.9520; all close to 1, showing that the fitted models explain well the observed data.

4. Early prediction of elbows

A real-word challenge is how to predict the trajectory of IR growth, e.g. the elbow points in IR curves as to detect early signs of unacceptable degradation. For example, to filter out cell production lots that exhibit poorer IR/capacity degradation trends. We complement the previous section in scope
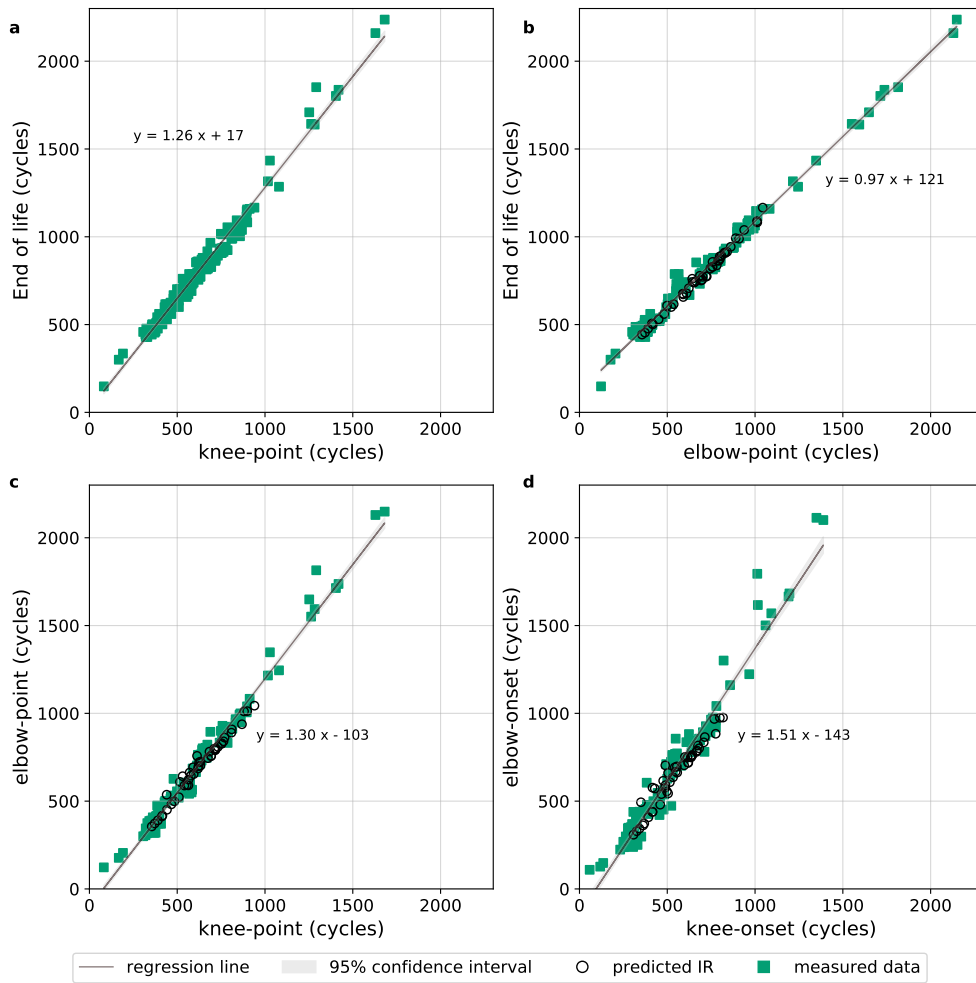
Figure 6. a, Linear regression models linking the knee-point to End of life. **b**, Linear regression model linking elbow-point to End of life. **c**, Linear regression model linking knee-point to elbow-point. **d**, Linear regression model linking knee-onset to elbow-onset. Every linear model is presented with a 95% confidence band on the plotted regression line, all linear relations here are calculated from the A123 dataset enriched with the predicted IR data for batch 8. Elbow points derived from the predicted IR data are highlighted as open black circles, the reader will appreciate that their inclusion did not significantly influence the linear regression results obtained.

of the findings of [20, Section 3]. We apply the quantitative knee prediction algorithm developed there to the early prediction of elbows without any additional optimization, i.e. 'as is'. A full description of the model and feature extraction process can be found in [20] and supplementary material, however, we provide a brief overview. It is outside the scope of this paper to revisit the early prediction of knees.

The quantitative prediction of the elbows is performed by a *Relevance Vector Machine (RVM)* [47], a type of linear regression mechanism, taking features extracted from the early life of the cells. The feature extraction process takes as input the first 50-cycles of the available per-cycle and in-cycle measurements (capacity, IR, charging-times, voltage, current, temperature) and draws on time-series analysis to calculate a vast collection of summary statistics without input from domain expertise (see [20, Supplementary Fig. 5]). Then, a sequential feature selection funnel is deployed to select around 100 features to train the RVM [20, Supplementary Figs. 6 and 7]. When using batch 8, the input IR is the predicted IR from Section 2.2.4 – the cases, with/without batch 8, are distinguished. The model is trained on data from all but one cell and tested on the remaining cells (leave-one-out framework), this

276 process is independently repeated such that each cell is used for testing once. The performance metrics
277 displayed in Table 5 are the average of the test performances.

278   The resultant early predictions are reported in Table 5 where two points should be made salient.
279 Firstly, on *elbows vs knees prediction* when comparing to [20], the model performs worse predicting
280 elbows than when predicting knees: MAPE 13.8% vs 12.0%, elbow-onset vs knee-onset, and MAPE
281 10.7% vs 9.4%, elbow-point vs knee-point – overall, the elbow prediction is up to 2% worse if compared
282 with knee prediction. This lower accuracy in elbow (vs knee) prediction was expected as the input IR
283 measurements are much noisier than the capacity measurements, and hence, as argued in Section 3.1,
284 the identification of elbows is inherently less exact [3] which turn affects the predictive performance.
285 Secondly, *on using the predicted IR data*, its inclusion leads to a marginally worse average performance
286 of our model: the MAPE worsens by 0.2% for the elbow-onset prediction and by less than 0.8% for the
287 elbow-point prediction, see Table 5. This critically showcases that the generated IR data may be used
288 for the prediction of elbows, which we emphasise was an input feature to the RVM.

(a) elbow-onset prediction

With b8?	Metric	Score	CI ($\alpha = 0.1$)
No	MAE (cycles)	89.1	[77.0, 101.8]
	MAPE (%)	13.8	[12.4, 15.3]
Yes	MAE (cycles)	91.3	[79.4, 104.0]
	MAPE (%)	14.0	[12.6, 15.5]

(b) elbow-point prediction

With b8?	Metric	Score	CI ($\alpha = 0.1$)
No	MAE (cycles)	76.3	[64.5, 88.6]
	MAPE (%)	10.7	[9.5, 12.0]
Yes	MAE (cycles)	83.4	[72.8, 94.6]
	MAPE (%)	11.5	[10.4, 12.8]

Table 5. Result of RVM regressor for elbow-onset (**a**) and elbow-point (**b**) when predictions are made
from the first 50 cycles. The 90% confidence intervals (CI) were calculated via bootstrapping. The entry
'*With b8?*' refers to results computed with ('Yes') and without ('No') the inclusion of the artificially
predicted IR data of batch 8.

289   From a methodological point of view, we employed the simple RVM algorithm of [20] in a direct
290 manner without any additional optimisation to take into account the noisier IR data or the predicted
291 IR data. This was a choice to prove that the generated IR data can be used for early prediction. There
292 is indeed room for future improvements in the early prediction of IR elbows and such is left for future
293 research. Lastly, increasing the number of cells displaying elbows by prediction to 169(=124+45) will
294 benefit approaches which are highly dependent on the size of a dataset.

5. Conclusions and future work

296   In this original work the IR rise curve of Li-ion cells is characterised by the novel concept of
297 'elbow-point' and 'elbow-onset'. A generalist identification algorithm is then proposed. In this regard,
298 the proposed approach is able to handle not only measurement noises but also sigmoid-type patterns
299 in capacity fade and IR rise curves. The findings highlight a strongly significant linear relationship
300 between EOL, capacity knee-point/IR elbow-point as well as capacity knee-onset/IR elbow-onset for
301 the data under study.

302   Two machine learning related goals were achieved. The first, part of the data pre-processing step,
303 draws on Neural Network techniques to build independent IR and capacity SOH predictors achieving
304 a small MAPE of 1.6% and 0.4% respectively, these results are of wider general interest. The proposed
305 IR estimator was deployed to complete an existing cell cycling dataset with missing IR measurements,
306 resulting in a well-rounded life cycle dataset encompassing capacity and IR data. The generated data
307 is publicly available. Such datasets can be used for both identification and early predictions of the

---

[3]   As demonstrated in Section 3.1, the confidence intervals for the elbow identification are significantly wider than those for
the knees. Due to this higher noise in the elbows, when predicting elbows from input data the relationship between input
data and elbows will be weaker/noisier than when predicting the knees.

elbows in IR curves. We provide an illustrative example for such an early predictor of IR elbows. Furthermore, the cells with predicted IR are shown to be usable for the early prediction of elbows, resulting in only slightly worse average performance than when they are excluded (the MAPE worsens by less than 0.8%).

The methods of elbow identification and prediction, in this work, have commercial value to battery manufacturers, as well as end users such as fleet managers and energy storage utility operators. Accurate early forecasting of the elbow (and knees) will allow manufacturers to set appropriate performance and lifetime warranties for their products. Additionally, elbow forecasting allows battery users to accurately and conveniently schedule battery servicing and replacement, or adjust the duty cycle to accommodate the reduced performance of the battery pack as it degrades.

In future, the accuracy of the early prediction will be enhanced. Multiple dimensions of inputs encompassing the predicted IR data and other measurements will be used to train the model with an improved tolerance for noisy data. Overall, elbow-identification and elbow early prediction can be used to influence the design of the thermal management system, accounting for the additional heat dissipated by cells as they approach their EOL. The early prediction of the IR elbow and onsets points in IR rise curves would determine the moment to taper down charging current in rapid charging protocols[4]. In addition, a fuller study comparing the relations between knee/elbow-onset and -point across more datasets is left for future work.

References

1. Gilbert, J.A.; Shkrob, I.A.; Abraham, D.P. Transition metal dissolution, ion migration, electrocatalytic reduction and capacity loss in lithium-ion full cells. *Journal of The Electrochemical Society* **2017**, *164*, A389–A399.

2. Waldmann, T.; Wilka, M.; Kasper, M.; Fleischhammer, M.; Wohlfahrt-Mehrens, M. Temperature dependent ageing mechanisms in lithium-ion batteries – A Post-Mortem study. *Journal of Power Sources* **2014**, *262*, 129 – 135.

3. Matsuda, T.; Ando, K.; Myojin, M.; Matsumoto, M.; Sanada, T.; Takao, N.; Imai, H.; Imamura, D. Investigation of the influence of temperature on the degradation mechanism of commercial nickel manganese cobalt oxide-type lithium-ion cells during long-term cycle tests. *Journal of Energy Storage* **2019**, *21*, 665–671.

4. Li, J.; Downie, L.E.; Ma, L.; Qiu, W.; Dahn, J. Study of the failure mechanisms of LiNi0. 8Mn0. 1Co0. 1O2 cathode material for lithium ion batteries. *Journal of The Electrochemical Society* **2015**, *162*, A1401–A1408.

---

[4] Arguably this tapering down would be done as soon as the cell hits its cut-off voltage, which it will do at an increasingly lower SOC as IR, and overpotential, increases.

5. Uitz, M.; Sternad, M.; Breuer, S.; Täubert, C.; Traußnig, T.; Hennige, V.; Hanzu, I.; Wilkening, M. Aging of tesla's 18650 lithium-ion cells: Correlating solid-electrolyte-interphase evolution with fading in capacity and power. *Journal of The Electrochemical Society* **2017**, *164*, A3503–A3510.

6. Campbell, I.D.; Marzook, M.; Marinescu, M.; Offer, G.J. How Observable Is Lithium Plating? Differential Voltage Analysis to Identify and Quantify Lithium Plating Following Fast Charging of Cold Lithium-Ion Batteries. *Journal of The Electrochemical Society* **2019**, *166*, A725–A739.

7. Park, K.J.; Hwang, J.Y.; Ryu, H.H.; Maglia, F.; Kim, S.J.; Lamp, P.; Yoon, C.S.; Sun, Y.K. Degradation Mechanism of Ni-Enriched NCA Cathode for Lithium Batteries: Are Microcracks Really Critical? *ACS Energy Letters* **2019**, *4*, 1394–1400.

8. Birkl, C.R.; Roberts, M.R.; McTurk, E.; Bruce, P.G.; Howey, D.A. Degradation diagnostics for lithium ion cells. *Journal of Power Sources* **2017**, *341*, 373–386.

9. Liu, Q.; Du, C.; Shen, B.; Zuo, P.; Cheng, X.; Ma, Y.; Yin, G.; Gao, Y. Understanding undesirable anode lithium plating issues in lithium-ion batteries. *RSC Advances* **2016**, *6*, 88683–88700.

10. Dubarry, M.; Baure, G.; Devie, A. Durability and reliability of EV batteries under electric utility grid operations: path dependence of battery degradation. *Journal of The Electrochemical Society* **2018**, *165*, A773–A783.

11. Somerville, L.; Bareño, J.; Trask, S.; Jennings, P.; McGordon, A.; Lyness, C.; Bloom, I. The effect of charging rate on the graphite electrode of commercial lithium-ion cells: A post-mortem study. *Journal of Power Sources* **2016**, *335*, 189 – 196.

12. Gao, Y.; Jiang, J.; Zhang, C.; Zhang, W.; Ma, Z.; Jiang, Y. Lithium-ion battery aging mechanisms and life model under different charging stresses. *Journal of Power Sources* **2017**, *356*, 103 – 114.

13. Hendricks, C.; Williard, N.; Mathew, S.; Michael, P. A failure modes, mechanisms, and effects analysis (FMMEA) of lithium-ion batteries. *Journal of Power Sources* **2015**, *297*, 113–120.

14. Friedrich, F.; Strehle, B.; Freiberg, A.T.S.; Kleiner, K.; Day, S.J.; Erk, C.; Piana, M.; Gasteiger, H.A. Capacity Fading Mechanisms of NCM-811 Cathodes in Lithium-Ion Batteries Studied by X-ray Diffraction and Other Diagnostics. *Journal of the Electrochemical Society* **2019**, *166*, A3760–A3774.

15. Rodrigues, M.T.F.; Kalaga, K.; Trask, S.E.; Dees, D.W.; Shkrob, I.A.; Abraham, D.P. Fast Charging of Li-Ion Cells: Part I. Using Li/Cu Reference Electrodes to Probe Individual Electrode Potentials. *Journal of the Electrochemical Society* **2019**, *166*, A996–A1003.

16. Shkrob, I.A.; Rodrigues, M.T.F.; Dees, D.W.; Abraham, D.P. Fast Charging of Li-Ion Cells: Part I. Using Li/Cu Reference Electrodes to Probe Individual Electrode Potentials. *Journal of the Electrochemical Society* **2019**, *166*, A3305–A3313.

17. Ahmed, S.; Bloom, I.; Jansen, A.N.; Tanim, T.; Dufek, E.J.; Pesaran, A.; Burnham, A.; Carlson, R.B.; Dias, F.; Hardy, K.; Keyser, M.; Kreuzer, C.; Markel, A.; Meintz, A.; Michelbacher, C.; Mohanpurkar, M.; Nelson, P.A.; Robertson, D.C.; Scoffield, D.; Shirk, M.; Stephens, T.; Vijayagopal, R.; Zhang, J. Enabling fast charging - A battery technology gap assessment. *Journal of Power Sources* **2017**, *367*, 250–262.

18. Yang, X.G.; Zhang, G.; Ge, S.; Wang, C.Y. Fast charging of lithium-ion batteries at all temperatures. *PNAS* **2018**, *115*, 7266–7271.

19. Severson, K.; Attia, P.; Jin, N.; Perkins, N.; Jiang, B.; Yang, Z.; Chen, M.; Aykol, M.; Herring, P.; Fraggedakis, D.; Bazant, M.; Harris, S.; Chueh, W.; Braatz, R. Data-driven prediction of battery cycle life before capacity degradation. *Nature Energy* **2019**, *4*, 1–9. doi:10.1038/s41560-019-0356-8.

20. Fermín, P.; McTurk, E.; Allerhand, M.; Medina-Lopez, E.; Anjos, M.F.; Sylvester, J.; dos Reis, G. Identification and machine learning prediction of knee-point and knee-onset in capacity degradation curves of lithium-ion cells. *Energy and AI* **2020**, p. 100006.

21. Raj, T.; Wang, A.A.; Monroe, C.W.; Howey, D. Investigation of Path Dependent Degradation in Lithium-Ion Batteries. *Batteries & Supercaps* **2020**.

22. Bao, Y.; Dong, W.; Wang, D. Online internal resistance measurement application in lithium ion battery capacity and state of charge estimation. *Energies* **2018**, *11*, 1073.

23. Diao, W.; Saxena, S.; Han, B.; Pecht, M. Algorithm to Determine the Knee Point on Capacity Fade Curves of Lithium-Ion Cells. *Energies* **2019**, *12*, 2910.

24. Neubauer, J.; Pesaran, A. The ability of battery second use strategies to impact plug-in electric vehicle prices and serve utility energy storage applications. *Lancet* **2011**, *196*, 10351–10358. doi:10.1016/j.jpowsour.2011.06.053.

25. Ecker, M.; Nieto, N.; Käbitz, S.; Schmalstieg, J.; Blanke, H.; Warnecke, A.; Sauer, D.U. Calendar and cycle life study of Li(NiMnCo)O2-based 18650 lithium-ion batteries. *Journal of Power Sources* **2014**, *248*, 839 – 851.

26. Han, X.; Ouyang, M.; Lu, L.; Jianqiu, L. Cycle Life of Commercial Lithium-Ion Batteries with Lithium Titanium Oxide Anodes in Electric Vehicles. *Energies* **2014**, *7*, 4895–4909.

27. Satopaa, V.; Albrecht, J.; Irwin, D.; Raghavan, B. Finding a "kneedle" in a haystack: Detecting knee points in system behavior. 2011 31st international conference on distributed computing systems workshops. IEEE, 2011, pp. 166–171.

28. Schuster, S.F.; Bach, T.; Fleder, E.; Müller, J.; Brand, M.; Sextl, G.; Jossen, A. Nonlinear aging characteristics of lithium-ion cells under different operational conditions. *Journal of Energy Storage* **2015**, *1*, 44 – 53.

29. Zhang, C.; Wang, Y.; Gao, Y.; Wang, F.; Mu, B.; Zhang, W. Accelerated fading recognition for lithium-ion batteries with Nickel-Cobalt-Manganese cathode using quantile regression method. *Applied Energy* **2019**, *256*, 113841.

30. Attia, P.M.; Grover, A.; Jin, N.; Severson, K.A.; Markov, T.M.; Liao, Y.H.; Chen, M.H.; Cheong, B.; Perkins, N.; Yang, Z.; others. Closed-loop optimization of fast-charging protocols for batteries with machine learning. *Nature* **2020**, *578*, 397–402.

31. Jones, E.; Oliphant, T.; Peterson, P.; others. SciPy: Open source scientific tools for Python, 2001–. [Online; accessed].

32. Kohavi, R.; others. A study of cross-validation and bootstrap for accuracy estimation and model selection. IJCAI'95: Proceedings of the 14th international joint conference on Artificial intelligence. Montreal, Canada, 1995, Vol. 2, pp. 1137–1143.

33. Chollet, F.; others. Keras: The python deep learning library. *ascl* **2018**, pp. ascl–1806.

34. Liang, K.; Zhang, Z.; Liu, P.; Wang, Z.; Jiang, S. Data-driven ohmic resistance estimation of battery packs for electric vehicles. *Energies* **2019**, *12*, 4772.

35. Remmlinger, J.; Buchholz, M.; Meiler, M.; Bernreuter, P.; Dietmayer, K. State-of-health monitoring of lithium-ion batteries in electric vehicles by on-board internal resistance estimation. *Journal of Power Sources* **2011**, *196*, 5357–5363.

36. Guha, A.; Patra, A. State of health estimation of lithium-ion batteries using capacity fade and internal resistance growth models. *IEEE Transactions on Transportation Electrification* **2017**, *4*, 135–146.

37. Tseng, K.H.; Liang, J.W.; Chang, W.; Huang, S.C. Regression models using fully discharged voltage and internal resistance for state of health estimation of lithium-ion batteries. *energies* **2015**, *8*, 2889–2907.

38. Giordano, G.; Klass, V.; Behm, M.; Lindbergh, G.; Sjöberg, J. Model-based lithium-ion battery resistance estimation from electric vehicle operating data. *IEEE Transactions on Vehicular Technology* **2018**, *67*, 3720–3728.

39. Saha, B.; Goebel, K.; Poll, S.; Christophersen, J. Prognostics methods for battery health monitoring using a Bayesian framework. *IEEE Transactions on instrumentation and measurement* **2009**, *58*, 291–296.

40. Zhang, J.; Zhang, X. A Novel Internal Resistance Curve Based State of Health Method to Estimate Battery Capacity Fade and Resistance Rise. 2020 IEEE Transportation Electrification Conference & Expo (ITEC). IEEE, 2020, pp. 575–578.

41. Qin, T.; Zeng, S.; Guo, J. Robust prognostics for state of health estimation of lithium-ion batteries based on an improved PSO–SVR model. *Microelectronics Reliability* **2015**, *55*, 1280–1284.

42. Ng, M.F.; Zhao, J.; Yan, Q.; Conduit, G.J.; Seh, Z.W. Predicting the state of charge and health of batteries using data-driven machine learning. *Nature Machine Intelligence* **2020**, pp. 1–10.

43. Pedregosa, F.; Varoquaux, G.; Gramfort, A.; Michel, V.; Thirion, B.; Grisel, O.; Blondel, M.; Prettenhofer, P.; Weiss, R.; Dubourg, V.; Vanderplas, J.; Passos, A.; Cournapeau, D.; Brucher, M.; Perrot, M.; Duchesnay, E. Scikit-learn: Machine Learning in Python. *Journal of Machine Learning Research* **2011**, *12*, 2825–2830.

44. Chakravarti, N. Isotonic median regression: a linear programming approach. *Mathematics of operations research* **1989**, *14*, 303–308.

45. Hu, C.; Ye, H.; Jain, G.; Schmidt, C. Remaining useful life assessment of lithium-ion batteries in implantable medical devices. *Journal of Power Sources* **2018**, *375*, 118–130.

46. Tang, X.; Liu, K.; Wang, X.; Gao, F.; Macro, J.; Widanage, W.D. Model migration neural network for predicting battery aging trajectories. *IEEE Transactions on Transportation Electrification* **2020**.

47. Bishop, C.M., Sparse Kernel Machines. In *Pattern recognition and machine learning*; Springer, 2006; chapter 7, pp. 325–353.

Supplementary Materials: The predicted Internal Resistance dataset created to complement Batches 4–8, those of the [30] dataset, is available online at https://doi.org/10.7488/ds/2957 .

Publisher's Note: MDPI stays neutral with regard to jurisdictional claims in published maps and institutional affiliations.